Subpixel heterogeneity of ice-wedge polygonal tundra: a multi-scale analysis of land cover and evapotranspiration in the Lena River Delta, Siberia

By S. MUSTER[1]*, M. LANGER[1], B. HEIM[1], S. WESTERMANN[2] and J. BOIKE[1],
[1]*Alfred-Wegener-Institute for Polar and Marine Research, Telegrafenberg A43, 14473 Potsdam, Germany;*
[2]*Department of Geosciences, University of Oslo, P.O. Box 1047, Blindern, 0316 Oslo, Norway*

ABSTRACT

Ignoring small-scale heterogeneities in Arctic land cover may bias estimates of water, heat and carbon fluxes in large-scale climate and ecosystem models. We investigated subpixel-scale heterogeneity in CHRIS/PROBA and Landsat-7 ETM+ satellite imagery over ice-wedge polygonal tundra in the Lena Delta of Siberia, and the associated implications for evapotranspiration (ET) estimation. Field measurements were combined with aerial and satellite data to link fine-scale (0.3 m resolution) with coarse-scale (up to 30 m resolution) land cover data. A large portion of the total wet tundra (80%) and water body area (30%) appeared in the form of patches less than 0.1 ha in size, which could not be resolved with satellite data. Wet tundra and small water bodies represented about half of the total ET in summer. Their contribution was reduced to 20% in fall, during which ET rates from dry tundra were highest instead. Inclusion of subpixel-scale water bodies increased the total water surface area of the Lena Delta from 13% to 20%. The actual land/water proportions within each composite satellite pixel was best captured with Landsat data using a statistical downscaling approach, which is recommended for reliable large-scale modelling of water, heat and carbon exchange from permafrost landscapes.

Keywords: permafrost, remote sensing, Arctic, wetlands, patterned ground, latent heat fluxes

1. Introduction

Arctic terrestrial ecosystems affect the earth's climate system through the exchange of water and energy regionally, and the exchange of long-lived greenhouse gases globally (Chapin et al., 2000). The exchange of water, energy and carbon between the surface and the atmosphere is determined by biogeophysical properties of the surface such as hydrology or albedo, as well as biogeochemical properties such as biomass, and vegetation type (Bonan et al., 1995; Chapin et al., 2005; McGuire et al., 2007). In both regional and global land surface and climate models, the biogeophysical parameters are estimated on the basis of land cover classifications. For large areas, these land cover classifications are derived from satellite systems such as MODIS or AVHHR. Their resolutions between 250 m and 1 km do not resolve surface heterogeneities with dimensions

over a few metres or even tens of metres. Fine-scale landscape heterogeneity on the scale of metres results in satellite pixels whose spectral characteristics are a composite of the different land cover types within the area covered by each pixel (Lillesand et al., 2004). This is especially true for patterned ground, which is a common phenomenon of the Arctic land surface (French, 2007; Walker et al., 2008). Ice-wedge polygonal tundra, for example, forms a network of small polygonal ponds and patches of wet or dry tundra that are 5–20 m in diameter. Such features cover large areas in the Arctic coastal plains of Alaska, in the Canadian Mackenzie delta and in the low-lying wetlands of northern Siberia (Tarnocai and Zoltai, 1988; Ping et al., 2004; Naumov, 2004). The various polygonal landscape elements have distinctly different water, heat and carbon fluxes. Wet tundra and overgrown water have been found to have the highest summer methane flux (Kutzbach et al., 2004; Sachs et al., 2010). Small water bodies show sensible and latent heat fluxes that are significantly different from the surrounding tundra in summer and winter (Langer et al.,

*Corresponding author.
email: sina.muster@awi.de

1

2011a). Our understanding of the influence that these local effects have on large-scale models, however, remains limited (Chapin et al., 2000). Whether and to which extent the aggregation of such fine-scale land cover heterogeneity introduces errors and uncertainties into extrapolation and model schemes remains a crucial matter for further research (Salmun et al., 2009). Moreover, the directions and magnitudes of these feedbacks are in a constant process of change as a result of the rapidly warming Arctic climate (Serreze et al., 2000; Hinzman et al., 2005). The resulting land surface changes in the Arctic coastal plain include an increase in the above-ground biomass through, for example, increased shrub cover (Sturm et al., 2001; Hinzman et al., 2005), prolongation of the snow-free season (Chapin et al., 2005) and changes in the surface water balance (Hinzman et al., 2005).

Evapotranspiration (ET), or latent heat flux, plays a key role in coupling the water and energy budget in Arctic wetlands underlain by permafrost such as the Lena Delta. Together, the precipitation (P) and the ET determine the net moisture input to a surface (P-ET), which consequently affects the water fluxes and storage. Regional and local variations of P-ET affect the duration and degree of wetland saturation (Boike et al., 2008; Woo et al., 2008) with implications for the freshwater budget of the Arctic Ocean (Kattsov et al., 2007; White et al., 2007) as well as the regional and local atmospheric circulation (Rouse, 2000; Rouse et al., 2003; Serreze et al., 2003; Gutowski et al., 2007; Woo et al., 2008). Precipitation and ET measurements are, however, sparse despite recent efforts to establish a circum-Arctic network of flux measurement stations (Euskirchen and Bret-Harte, 2009). The current distribution patterns of precipitation and ET therefore remain largely uncertain, rendering any evaluation of recent variations and trends extremely difficult (Serreze et al., 2003; Kattsov et al., 2007; Woo et al., 2008).

In this study we have investigated the effect of fine-scale variations in land cover on ET from mid-summer to late fall in ice-wedge polygonal tundra in the Siberian Lena Delta. We used a multi-scale data set of field-based measurements together with aerial and satellite data to scale land cover and ET from the plot ($0.1–100\,m^2$) to the landscape scale ($100–10^6\,m^2$). The objectives of the study were (1) to map the spatial variability in land cover and ET in ice-wedge polygonal tundra, (2) to assess the subpixel-scale spatial heterogeneity of CHRIS/PROBA and Landsat-7 ETM + satellite imagery and (3) to consider the implications of subpixel-scale variability for the landscape-scale estimation of water, energy and carbon fluxes in general, and ET in particular. In the end, we present an empirical downscaling approach for incorporating fine-scale land cover patterns into coarse-scale climate and ecosystem models.

2. Study area

The study area is located on Samoylov Island in the Lena River Delta, 120 km South of the Arctic Ocean (72°22′N, 126°30′E) (Fig. 1a). The Lena Delta is the largest river delta in the Arctic, covering an area of about $29\,036\,km^2$ (Schneider et al., 2009), of which $21\,719\,km^2$ represent land and the remaining areas are occupied by rivers and coastal zones. It forms a wetland complex that is dominated by sedges, grasses, mosses and dwarf-shrubs less than 40 cm high (Walker et al., 2005). The region is characterised by an arctic-continental climate with a mean annual air temperature of about $-13\,°C$ and a mean annual precipitation of about 140 mm. Snow melt usually starts at the beginning of June, and the growing season lasts from mid-June to mid-September (Boike et al., 2008). The region is underlain by continuous permafrost that reaches depths of 500–600 m (Grigoriev, 1960).

Three main geomorphological units, i.e. river terraces, were identified in the Lena Delta (Grigoriev, 1993; Schwamborn et al., 2002) (Fig. 1b). Samoylov Island is located on the first terrace (1–12 m a.s.l.), which was formed during the Middle Holocene and occupies most of the central and eastern parts of the delta with a surface area of about $15\,840\,km^2$ (Morgenstern et al., 2008). The first terrace is characterised by ice-wedge polygonal tundra together with large thermokarst lakes and active flood plains, and features relatively ice-rich sediments. The second terrace (20–30 m a.s.l.) in the north-western part of the delta formed between the Late Pleistocene and Early Holocene and is characterised by sandy sediments with a low ice content. It shows little polygonal relief but features many large thermokarst lakes. The third and oldest terrace (30–55 m a.s.l.) is an erosional remnant of a Late Pleistocene plain consisting of fine-grained, organic-rich and ice-rich sediments characterised by polygonal ground and thermokarst processes.

Samoylov Island consists of an active floodplain in the West ($1.49\,km^2$) that is flooded annually during spring and an elevated river terrace ($2.85\,km^2$) in the East (Fig. 1c). The terrace is characterised by large thermokarst lakes (larger than 10 ha) surrounded by ice-wedge polygonal tundra. It has an extremely low-gradient landscape relief with slopes of less than 0.2%. The ice-wedge polygons, however, form a prominent microrelief: the growth of ice wedges in frost cracks leads to raised rims on either side of the crack, which are between 0.2 m and 1.0 m higher than the low-lying polygon centres. The water table is close to the surface, and drainage is greatly impeded by the underlying permafrost, resulting in water-saturated soils or inundated depressed polygon centres, whereas the elevated rims and any high-centred polygons are relatively dry. High-centred polygons are typically found along the lake
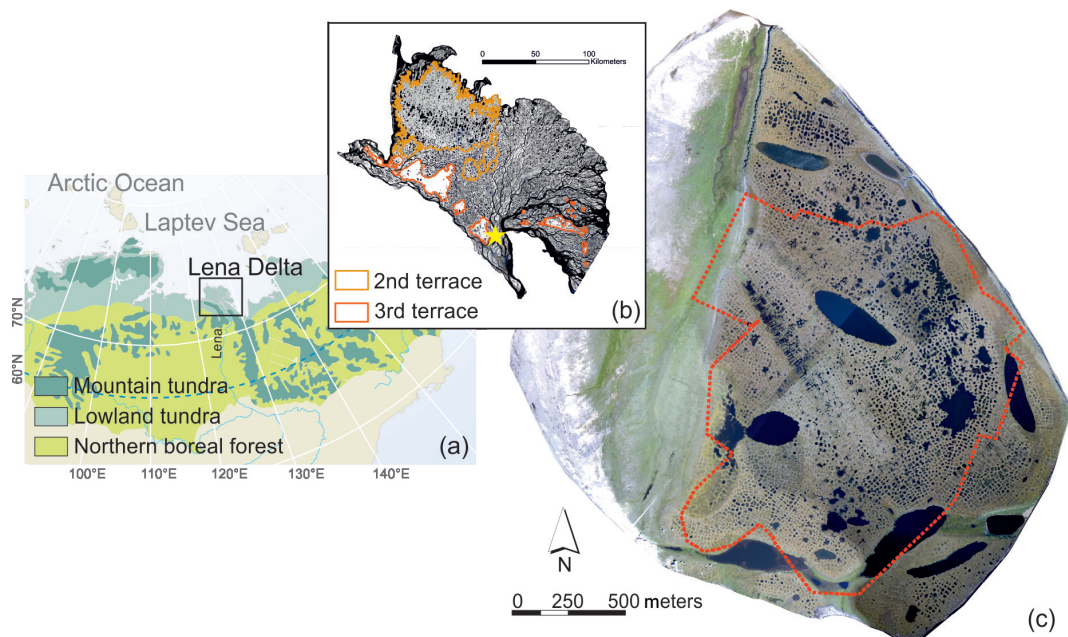
Fig. 1. (a) Location of the Lena River Delta in northern Siberia. (modified from *Vegetation zones in the Arctic – UNEP/GRID-Arendal Maps and Graphics Library*). (b) Near-infrared Landsat mosaic of the Lena River Delta. The third terrace of the delta is outlined in orange and the second terrace in red, with the remaining area representing the first terrace. The yellow star indicates the location of Samoylov Island on the first terrace. (c) Aerial image mosaic of Samoylov Island with a flood plain in the West and an elevated river terrace in the East. The red dotted line indicates the total mapped area of ice-wedge polygonal tundra.

margins and on elevated plateaus. In the following, we refer to inundated ice-wedge polygonal centres as polygonal ponds, which are shallow water bodies with depths of 0.5–1 m.

Boike et al. (2008) and Langer et al. (2011a) conducted intensive studies into the water and energy balance on Samoylov Island. They found that about 50% of the available net radiation is consumed by the latent heat flux, while the sensible and the ground heat fluxes make about 20–30%. The maximum thaw depths reach 0.4–0.5 m during summer months. ET is a major component of the site's water and energy budget, ranging between 31% of the total water budget in dry years and 61% in wet years (Boike et al., 2008).

3. Methods

We used a multi-scale data set to upscale land cover and ET from the plot scale ($0.1–100\,\mathrm{m^2}$) to the landscape scale ($100–10^6\,\mathrm{m^2}$). Visible and near-infrared aerial imagery was used to map the land cover in the ice-wedge polygonal tundra of Samoylov Island with a sub-metre resolution. The total mapped area encompasses about $1.76\,\mathrm{km^2}$ of the polygonal tundra (Fig. 1c). The four land cover types mapped were *dry tundra*, *wet tundra*, *overgrown water* and *open water*. The aerial land cover classification was then compared with the spectral classification of CHRIS/ PROBA and Landsat-7 ETM+ satellite images with a resolution of 17 and 30 m, respectively (Fig. 2). The relative importance of each land cover type with regard to ET was also assessed. The plot scale ET from tundra surfaces was measured using manual and automatic lysimeters, while evaporation from ponds was modelled using available climate data. Plot scale estimates of ET were then compared with eddy covariance measurements using the high-resolution land cover classification over the eddy footprint area (Fig. 2). The lysimeter measurements, eddy covariance measurements and the other ancillary measurements overlapped both spatially and temporally with the remote sensing data (Table 1). The spatial distribution of measuring plots and stations is shown in Fig. 3.

3.1. Field measurements

3.1.1. Field-based land cover mapping. Mapping of the ice-wedge polygonal tundra on Samoylov Island identified the different land cover types on the basis of an extensive field inventory of vegetation composition, vegetation structure, microtopography, and near-surface moisture.

The vegetation survey, which was completed in the summer of 2006, followed the phytosociological approach of Braun-Blanquet (1932). Plant communities were recorded
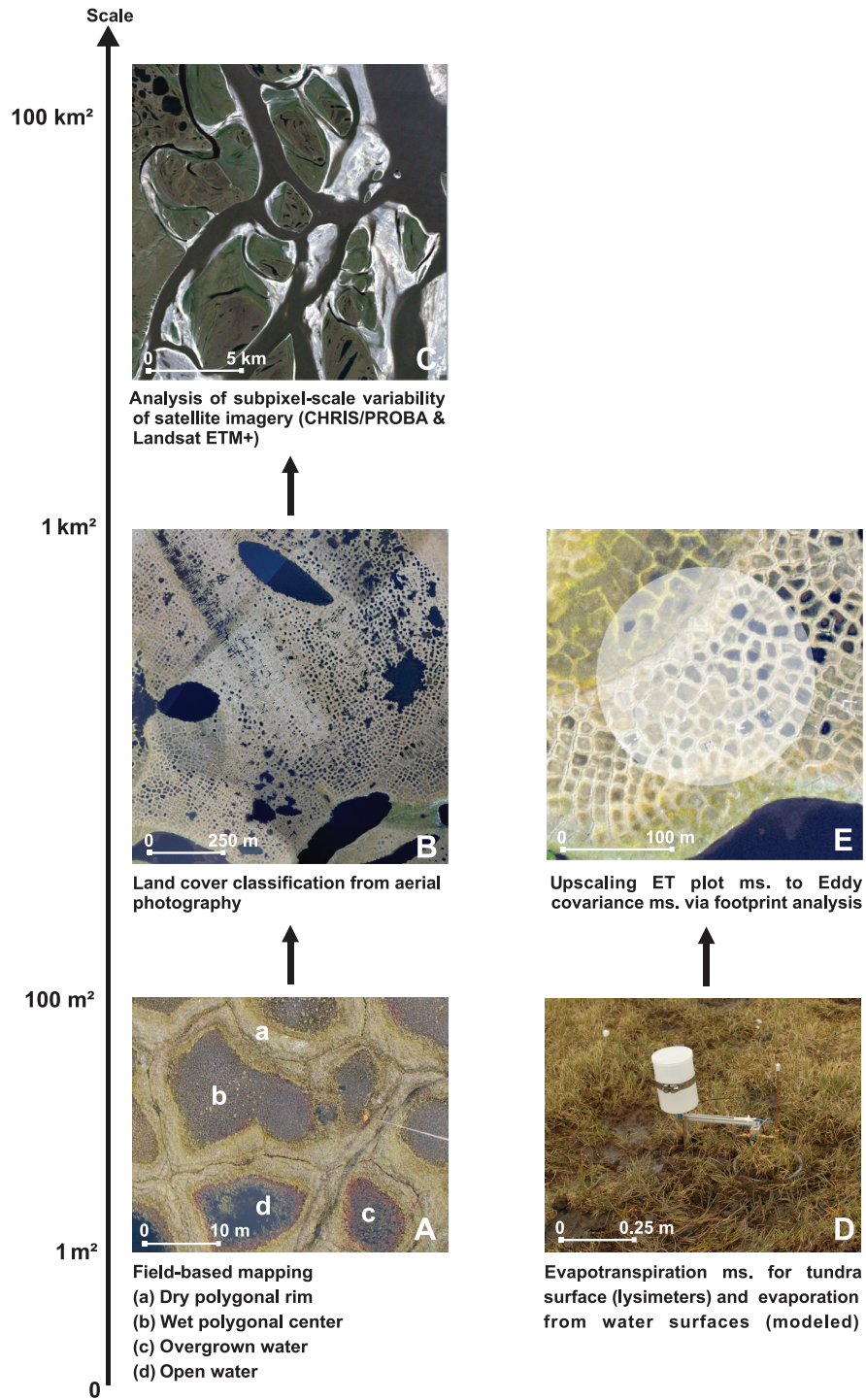
Fig. 2.   Scaling approach. Left-hand side: Upscaling land cover from (A) field-based mapping to (B) high-resolution land cover classification from aerial images and (C) satellite imagery. Domains (A), (B) and (C) show the effect of scale on extent and resolution as investigated in the study – from the plot scale with a high resolution but limited spatial extent (A, B) to the regional scale with low resolution but a large coverage (C). Right-hand side: Upscaling evapotranspiration (ET) rates from (D) plot measurements (ms) to eddy covariance measurements (E) through aerial land cover classification of the eddy footprint.

Table 1. Observation periods and the number of plots for field measurements of volumetric water content (VWC), evapotranspiration (ET) and vegetation surveys in *wet tundra* and *dry tundra*. Details of aerial and satellite data, including image acquisition dates.

	Date/time period	Number of plots
Field measurements		
VWC	August 13–September 24, 2008	Dry tundra: 11, wet tundra: 11
ET	July 21–September 14, 2008	Dry tundra: 7, wet tundra: 10
Vegetation survey	July 2006	Dry tundra: 51, wet tundra: 50
Imagery		
Aerial imagery	August 1, August 9 and August 15, 2008	
CHRIS/PROBA	July 23, 2008	
Landsat-7 ETM+, North and South of Delta, including area of study site	July 27, 2000	
Landsat-7 ETM+, West of Delta	July 26, 2001	

from 101 plots with relatively homogeneous vegetation and topography, with the plot sizes ranging from 12 to $100\,m^2$. Species presence and areal cover, i.e. the relative area covered by the different plant species in a plot, were assessed visually for each plot using the standard Braun-Blanquet scale. The plots were clustered according to species cover using the K-means2 partitioning program by Legendre (2001) in order to obtain vegetation types.

The volumetric water content (VWC) was measured daily from August 13 to September 24, 2008, in 11 polygon centres and on their adjacent rims by inserting a Campbell Hydrosense soil moisture sensor with a 12 cm fork vertically into the ground. Square plots (50×50 cm) of relatively homogeneous vegetation were identified at each site for the measurements, and the average of three measurements was recorded for each of the plots.

The microtopography of each measurement site was classified as elevated or collapsed polygon rim, elevated or depressed polygon centre and trench or crack.

3.1.2. ET measurements from lysimeters. ET from tundra surfaces was measured at the plot scale from July 21 to September 14, 2008, using both manual and automatic weighing lysimeters. Seventeen lysimeters were installed along a 1 km transect (Fig. 3), seven in wet polygon centres and ten on dry polygon rims.

Automatic lysimeters consisted of two cylindrical containers nested inside each other. The inner container had an internal diameter of 0.21 m and a height of 0.10 m. A load cell (Soemer 1006) was installed centrally at the base, between the inner and outer cylinders. This load cell had a measurement range of 2–5 kg with an accuracy of 0.03%: a 3-point calibration was conducted in the field. A sample of

the upper layer of soil and vegetation was excavated and carved by hand to fit into the inner cylinder, providing a relatively undisturbed sample. Automatic lysimeter weights were recorded every half hour using a CR1000 Campbell Scientific Logger. Mean daily values for the automatic lysimeters were calculated from noon to noon.

Manual lysimeters also consisted of two nested cylindrical containers, with internal dimensions of 0.14 m diameter and 0.12 m height. Weights from the manual lysimeters were recorded daily at noon using a Kern MH5K5 pocket balance, which had an accuracy of ± 5 g.

Measurements from manual lysimeters were rejected on days that had measurable precipitation, and those from automatic lysimeters were rejected for any periods of precipitation. The observed drying and wetting of the samples was in general agreement with the surrounding surface conditions throughout the observation period. Mean daily ET rates for both dry rims and wet centres were derived by averaging both manual and automatic lysimeter measurements, provided that at least three observations were available from the dry and wet sites, respectively. A total of 40 daily ET observations were thus obtained from *dry tundra* and 44 from *wet tundra* during the 56-d observation period.

3.1.3. Evaporation from water surfaces. We used a flux gradient approach to estimate evaporation (E) from small water bodies (smaller than 0.1 ha). The latent heat flux, Q_E, can be related to the difference between the specific humidity at the measurement height, $q(z_m)$, and at the water surface, $q(z_{surf})$, as follows:

$$Q_E = \frac{-\rho_{air} L_v}{r_a} (q(z_m) - q(z_{surf})), \qquad (1)$$

Land cover class
- ☐ Dry tundra
- ☐ Wet tundra
- ☐ Overgrown water
- ☐ Open water

Stations
- ☆ Eddy covariance station
- ● Lysimeter and soil moisture plots
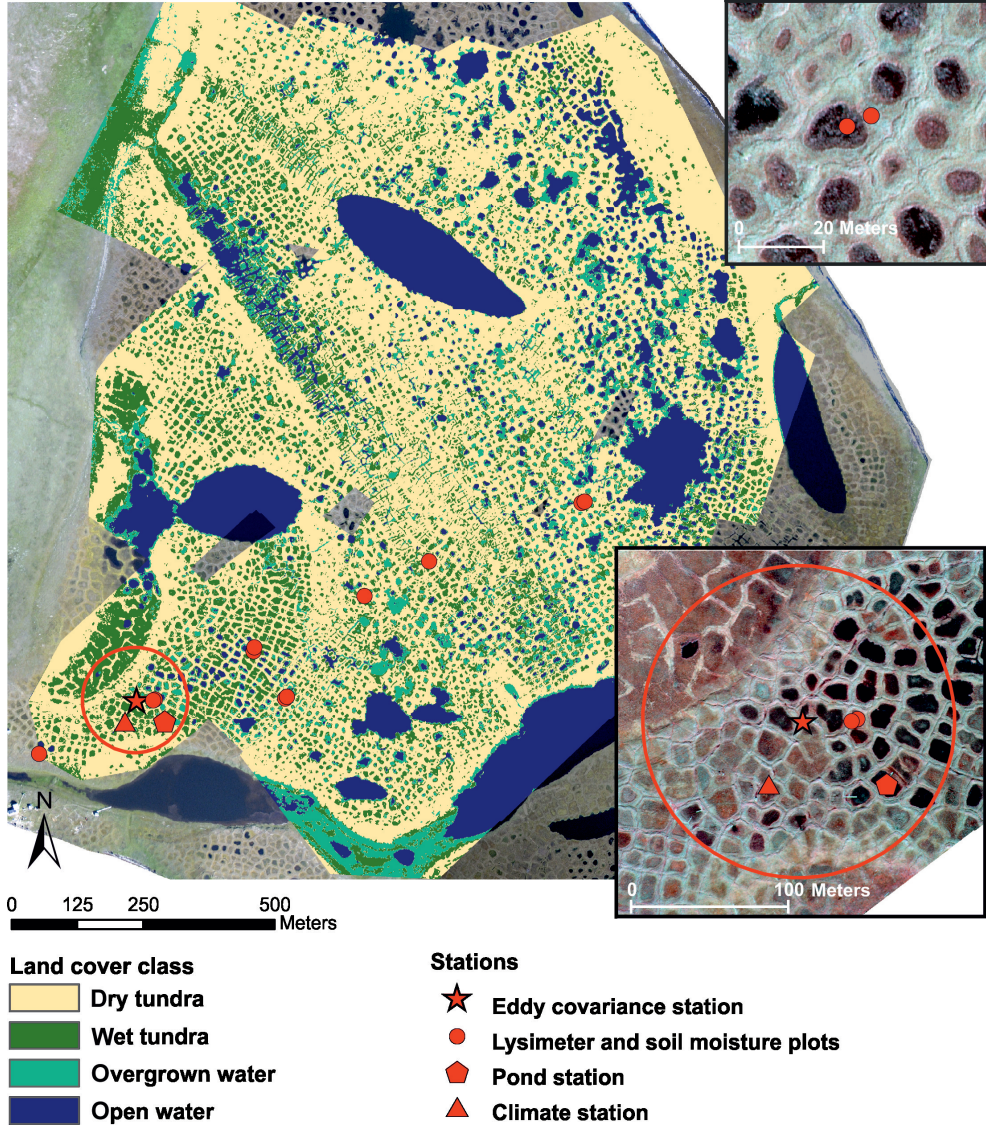- ⬠ Pond station
- △ Climate station

Fig. 3. (a) Aerial land cover classification of the ice-wedge polygonal tundra on Samoylov Island, showing the polygonal pattern of low-lying centres of *wet tundra* and polygonal ponds, separated by elevated polygonal rims of *dry tundra*. Locations of measurement stations are marked in red. The red circle indicates the approximate footprint area of the eddy covariance station. (b) Close-up view of a near-infrared aerial image showing a typical lysimeter and soil moisture measurement set-up with one lysimeter installed in a wet polygon centre and another one on a dry polygon rim. (c) Close-up view of the eddy footprint area and the measurement stations within.

where ρ_{air} is the density of air, L_v is the latent heat of vaporisation and r_a is the aerodynamic resistance (Garratt, 1994).

The specific humidity at a saturated surface, $q(z_{surf})$, can be inferred from the surface temperature, T_{surf}, using the Magnus formula, which gives the water vapour pressure over a water surface (Sonntag, 1990). The specific humidity of air, $q(z_m)$, at the measuring height, $(z_m = 2\,\text{m})$, is calculated from the air temperature, T_{air}, applying the Magnus formula in combination with the relative humidity, RH, at the measuring height.

The aerodynamic resistance, r_a, can be expressed as

$$r_a = \frac{\left[\ln\left(\frac{z_m}{z_0}\right)\right]^2}{\kappa^2 u_{zm}},\tag{2}$$

where u_{zm} is the horizontal wind speed at measuring height z_m, $\kappa = 0.4$ is the von Kármán constant, and $z_0 = 10^{-4}\,\text{m}$ is the roughness length for a calm water surface (Garratt, 1994). Equation (2) is only valid for neutral conditions, which dominated the atmospheric stratification at the study site in 2008 (Langer et al., 2011a), and provides a

first-order approximation for the turbulence characteristics at this site.

E (mm) is related to Q_E through the latent heat of vaporisation, L_v, as follows:

$$Q_E = \rho_{air} L_v E. \tag{3}$$

The water surface temperature was measured about 1 cm below the water surface of a shallow polygonal pond (total depth of about 0.8 m) using a PT100 temperature sensor, protected from radiation. We considered these water temperatures to be representative of all small water bodies with a surface area of less than 0.1 ha. Air temperature was measured in 2 m height at the eddy covariance measurement site, again using a PT100 sensor. Both PT100 sensors had an accuracy of 0.1–0.2 °C. Relative humidity was measured at the eddy covariance measurement site using an MP-100 humidity-temperature meteorological probe with an accuracy of $\pm 1\%$ (Rotronic, Switzerland). Daily mean values were used for all parameters in order to calculate evaporation. The evaporation model was applied to both surfaces of *open water* and *overgrown water* (with up to 15% areal plant cover).

3.1.4. ET measurements from eddy covariance.

3.1.4. ET measurements from eddy covariance. The ET at the landscape scale was determined using the eddy covariance method in summer 2008, as described by Langer et al. (2011a). The eddy covariance system consisted of a Campbell C-SAT 3D sonic anemometer and an open path LI-COR LI-7500 CO_2 and H_2O gas analyser mounted on a 2.4 m mast. Data were processed according to a standard quality assessment (Mauder and Foken, 2004; Mauder et al., 2008), resulting in an estimated measurement accuracy for ET of about 15% (Mauder et al., 2006). The quality assessment resulted in a data reduction of about 4%. A further data reduction of about 14% occurred as a result of exclusion of the area on the leeward side of the mast (263–277°). No gap filling was applied. Missing values were randomly distributed throughout the eddy data set, and we therefore considered the average latent heat flux value to be representative for the observation period. Further details on the measurement equipment setup and data processing can be found in the study by Langer et al. (2011a).

The source area for the latent heat flux was determined for each half-hour value using the footprint model of Schmid (1994). A constant aerodynamic roughness length of $z_0 = 10^{-3}$ m was assumed for the area of the footprint that included both tundra and water surfaces. The average footprint for the observation period broadly resembled a circle with a diameter of 100 m, as shown in Fig. 2. During the observation period from July to September 2008, wind directions showed only a slight predominance in the NW and ESE directions, and ratios of land cover types within the footprints showed only minor variations ($\pm 5\%$) (Langer et al., 2011a).

Ancillary measurements were collected at a standard climate tower in the vicinity of the eddy covariance system, including net radiation (using a CNR1 Net Radiometer from Kipp & Zonen, Netherlands) with an accuracy of 10%, and precipitation (using a tipping bucket rain gauge – Model 52203 from R.M. Young Company, USA) with an accuracy of 2% (Boike et al., 2008).

3.1.5. Upscaling ET measurements. A 'measure and multiply' approach was used to extrapolate the plot measurements of ET per unit area for each land cover type to the eddy footprint area and to the total mapped area of ice-wedge polygonal tundra on Samoylov Island (Fig. 3). The total ET over *i* land cover types was calculated using

$$ET = \sum (\%A_i \times ET_i), \tag{4}$$

where ET is the total ET, A_i is the total area of land cover type *i*, and ET_i is the ET per unit area from the land cover type *i*. Areally weighted plot-scale measurements of ET for the eddy footprint were then compared with the measured eddy covariance data.

3.2. Remote sensing data

3.2.1. Aerial imagery. We obtained sub-metre resolution aerial images of Samoylov Island by mounting two Nikon D200 cameras on a helium-filled dirigible. Images were acquired in the visible (VIS) and near-infrared (NIR) ranges (together referred to as the VNIR range). The internal IR-filters were removed from the cameras in a laboratory (LPD LLC, USA), allowing them to capture a maximum range from about 330 to 1200 nm. A Schneider Kreuznach B + W 486 UV-IR cut filter was used for one of the cameras to obtain images in the VIS range, from about 400 to 690 nm, while the second camera was fitted with a Schneider Kreuznach B + W IR-filter 093 to acquire images in the NIR range, above about 830 nm.

The flights took place at noon on sunny, cloudless days (August 1, August 9 and August 15, 2008). The total precipitation during the flying period (from July 31 to August 15) was 6.5 mm, with a daily maximum of 1.6 mm on August 10 (Fig. 5). An average flying altitude of 750 m resulted in a pixel size of about 0.18 m.

The aerial image data were processed using ENVI 4.7 image processing software. NIR images were registered onto VIS images using the automatic image-to-image registration with an average root mean square error (RMSE) of 0.53 pixels. The resulting VNIR images were then georeferenced using an orthomosaic of the island from

2007 with a resolution of 0.3 m. We chose the nearest neighbour algorithm for all resampling operations.

Sixteen images were used to map the ice-wedge polygonal tundra on Samoylov Island, with an image overlap of about 25%. Land cover classification was carried out individually for each VNIR image. *Open water* surfaces were extracted using a density slice classification applied to the NIR band. The NIR range is especially suited for detecting water bodies, as most of the incoming energy is absorbed and thus a marked difference exists between the reflectance from *open water* surfaces and that from vegetated surfaces. We chose a threshold that most effectively separated the image pixel values for water from those for vegetated surfaces. *Open water* surfaces were subsequently masked, and the remaining three vegetated land cover types, i.e. *wet tundra*, *dry tundra* and *overgrown water*, were classified using a supervised maximum likelihood classifier. Training areas and areas for accuracy assessment were selected from field-based mapping completed in 2006, 2008 and 2010. The relative classification accuracy was calculated by comparing the classifications for overlapping areas of adjacent images. In order to determine the overall classification accuracy, we compared a total of 147 ground-based plots to the final aerial land cover classification. Spurious pixels within a class were changed to conform to that class by applying a majority filter of 11×11 pixels. Areas smaller than 0.5×0.5 m were not included in subsequent analyses.

3.2.2. Satellite imagery. We used CHRIS/PROBA imagery with a resolution of 17 m per pixel, and Landsat-7 ETM + imagery with a resolution of 30 m, to investigate the effect of coarse resolutions on land cover mapping in ice-wedge polygonal tundra.

The CHRIS/PROBA image was acquired on July 23, 2008. The image was taken in CHRIS/PROBA operation mode 3, with 18 spectral bands covering the VNIR range from 400 to 1050 nm. The image was corrected for noise and atmospheric effects using the noise reduction (Gómez-Chova et al., 2008) and the atmospheric correction tool (Guanter et al., 2006) available in the BEAM VISAT 4.6.1 software.

An atmospherically corrected Landsat mosaic processed by Schneider et al. (2009) was used to classify the entire Lena Delta. Schneider et al. (2009) identified nine land cover classes for the Lena Delta, five of which are present in the ice-wedge polygonal tundra on Samoylov Island. We therefore performed classification for these five classes only, which together make up 70% of the total land area in the Lena Delta. The Landsat mosaic consists of three images acquired on July 27, 2000 (featuring Samoylov Island), and July 26, 2001. Bands 1–5 and band 7 were used

for classification covering a spectral range in the VNIR and short-wave infrared (SWIR) from 450 to 2350 nm.

Both the CHRIS/PROBA image and the Landsat mosaic were classified using a *k*-means unsupervised algorithm in the ENVI 4.7 software. Unsupervised classifications are based solely on the natural groupings within the image, i.e. the spectral properties of the surface, and as such return spectral classes containing spectrally similar pixels (Lillesand et al., 2004). The *k*-means algorithm is an iterative clustering algorithm that maximises the between-cluster variance and minimises the within-cluster variability (MacKay, 2003). The within-cluster variability is expressed as the sums of squared distances, SS, between each pixel *x* and its assigned cluster centre *C(x)* (MacKay, 2003):

$$SS = \sum_{\forall x} [x - C(x)]^2. \tag{5}$$

Classification was performed with 9 clusters and 15 iterations.

For Samoylov Island, we compared the satellite spectral classifications (*k*-means) from CHRIS/PROBA data and Landsat data with the aerial land cover classification, in order to assess the fine-scale land cover variability within each satellite pixel and *k*-means class. *k*-means classifications of the satellite data were registered onto the aerial land cover classification in ArcGIS 10, with an RMSE of less than 1 pixel.

4. Results

4.1. Land cover classification from field mapping

The ice-wedge polygonal tundra on Samoylov Island exhibits four distinct land cover types comprising two types of tundra and two types of water bodies. The tundra shows distinct characteristics related to microtopography and through variations in vegetation and surface wetness, which resulted in a classification of *dry tundra* or *wet tundra*. The *dry tundra* had a mean volumetric water content (VWC) of about 25% in the upper 10 cm of the soil, whereas the *wet tundra* had a mean VWC of about 93% throughout the observation period from August 13 to September 24, 2008. Both *dry tundra* and *wet tundra* did not show significant differences in VWC for the summer and fall period. *Dry tundra* was found on polygon ridges, well-drained plateaus and elevated polygon centres, while *wet tundra* was found in depressed polygon centres, in trenches and on collapsed ridges. Both *wet tundra* and *dry tundra* were dominated by mosses, which comprised up to 98% of the cover. They differed, however, with regard to key species and plant functional types (Table 2).

Water surfaces were classified as either *overgrown water* (with up to 15% areal plant cover) or *open water* with no

Table 2. Volumetric water content (VWC) of the upper surface (10 cm), plant functional types and key species for wet and *dry tundra*, derived from field measurements. The VWC is shown as the range of surface moisture (in percentages) across all plots, for *dry tundra* and *wet tundra*

	Dry tundra	Wet tundra
VWC [range in%]	7–51	55–100
Key species	*Hylocomium splendens,* *Dryas punctata*	*Drepanocladus revolvens, Meesia* *triquetra, Rhizomnium punctatum*
Plant functional type [cover in%]		
Moss	96	98
Forb	8	2
Shrub	3	1
Grass	2	1
Sedge	5	16
Lichen	2	Smaller than 1

emersed vegetation. *Overgrown water* was found in frost cracks and in polygon centres with transient water accumulations, as well as close to the banks of ponds and lakes.

4.2. Land cover classification from high-resolution aerial photography

High-resolution aerial photography during the observation period between July 21 and September 14, 2008, revealed the total mapped area of Samoylov Island to be composed of 58% *dry tundra*, 17% *wet tundra* and 25% water surfaces, thereof 10% *overgrown water* and 15% *open water* (Fig. 3a). Excluding large thermokarst lakes (larger than 0.1 ha), the ice-wedge polygonal tundra was composed of 65% *dry tundra*, 19% *wet tundra* and 16% water bodies (Table 3). The average footprint area of the eddy covariance station had a much higher proportion of *wet tundra* with 37% and a lower proportion of water bodies with 10%.

Both field observations and the aerial classification showed that the extent of surface water varied by about ±5% over the observation period, which is a negligible

figure compared to the overall classification accuracy. In areas where aerial photographs overlapped the land cover classification varied by about 3% on average. The overall accuracy of the classification was 84%, with the *open water* class showing the highest level of accuracy with 100%, followed by the *wet tundra* class with 91%. The *overgrown water* and *dry tundra* classes showed the lowest accuracy (62% and 75%, respectively) with most of the misclassified sites categorised as *wet tundra*.

In the discussions below we use the term water bodies to refer to both *overgrown* and *open water* with surface areas greater than 5 m². Water bodies ranged from ice-wedge polygonal ponds (smaller than 0.1 ha) to large thermokarst lakes (larger than 10 ha) with a mean surface area of 108 m². Polygonal ponds with a surface area between 0.003 and 0.1 ha are abundant in the ice-wedge polygonal tundra on Samoylov Island, amounting to 748 polygonal ponds per square kilometre. More than 90% of the total number of water bodies had a surface area less than 500 m². About 50% of the total number of water bodies had a surface area less than 10 m², but despite their large number they contributed only about 1% to the total water surface

Table 3. Land cover percentages and ET ratio for the eddy footprint, the total mapped area on Samoylov Island and the Lena Delta. Land cover percentages of the Lena Delta represent the subpixel-scale heterogeneity as derived from Fig. 7. Land surface percentages exclude water bodies with surface areas greater than 0.1 ha, i.e. water bodies that can be mapped directly with Landsat data. ET ratio is the contribution of the different land cover types to the areally weighted evapotranspiration based on the mean daily ET rates for the whole observation period as well as for the summer and fall period (Fig. 6).

Study area	Period	Land cover ratio [%]			ET ratio [%]		
		Dry tundra	Wet tundra	Water	ET_{dry}	ET_{wet}	E_{water}
Eddy footprint	Summer and fall	54	37	9	52	40	8
Samoylov Island	Summer and fall	65	19	16	65	21	14
Samoylov Island	Summer				53	29	18
Samoylov Island	Fall				79	13	9
Lena Delta		72	16	12			

area. Large thermokarst lakes were not common and represent less than 1% of the total number of water bodies, while contributing over 45% to the total water surface area (Fig. 4).

The frequency distribution of *wet tundra* patches was similar to the frequency distribution of water bodies, but the mean surface area of *wet tundra* patches was much smaller with $22.5 \, \text{m}^2$. About 99% of the *wet tundra* patches were smaller than $500 \, \text{m}^2$, making up 80% of the total surface area of *wet tundra*.

No mean patch size could be given for *dry tundra*. The aerial land cover classification did not resolve cracks and troughs in full detail, so that *dry tundra* appears as an interconnected surface of dry rims and high-centred polygons on the map, which together make up 94% of the total area of *dry tundra*.

4.3. Spatial and seasonal characteristics of ET

The observation period was characterised by two main synoptic periods: a relatively dry summer period (July 21 August 21) with low precipitation and high net radiation, followed by a period of frequent heavy rain events and low net radiation during the fall (August 22 to September 14)

(Fig. 5). The precipitation input (67 mm) and net evaporative output (68 mm) during the whole observation period were in overall balance. Negative latent heat fluxes were measured on 20 nights during the 56-d observation period with a mean of $-21.4 \, \text{W/m}^2$.

Evapotranspiration from *wet tundra* (ET_{wet}) and water bodies (E_{water}) was highest during the summer period (Fig. 6). E_{water} and ET_{wet} were higher than ET from *dry tundra* (ET_{dry}) by 40 and 80%, respectively. In summer, ET_{wet} was about 20% higher than E_{water}. Both E_{water} and ET_{wet} decreased from summer to fall by 52 and 57%, respectively, whereas ET_{dry} increased by 47%. ET_{dry} was twice as high than E_{water} and ET_{wet} in fall. Over the whole observation period, the effect of the different synoptic periods was cancelled out, and ET rates from *dry tundra* (1.2 mm/d with a standard deviation (SD) of 0.8 mm/d) were almost the same as ET rates from *wet tundra* (1.3 mm/d; SD = 0.9 mm/d) and water bodies (1.0 mm/d; SD = 0.6 mm/d).

ET rates of *wet tundra* and *dry tundra*, together with those for water bodies, were used to derive the area-weighted average ET rate of 1.2 mm/d (SD = 0.7 mm/d) for the eddy footprint. Direct measurements of ET using the eddy covariance system during the observation period showed an average rate of 1.2 mm/d (SD = 0.6 mm/d).
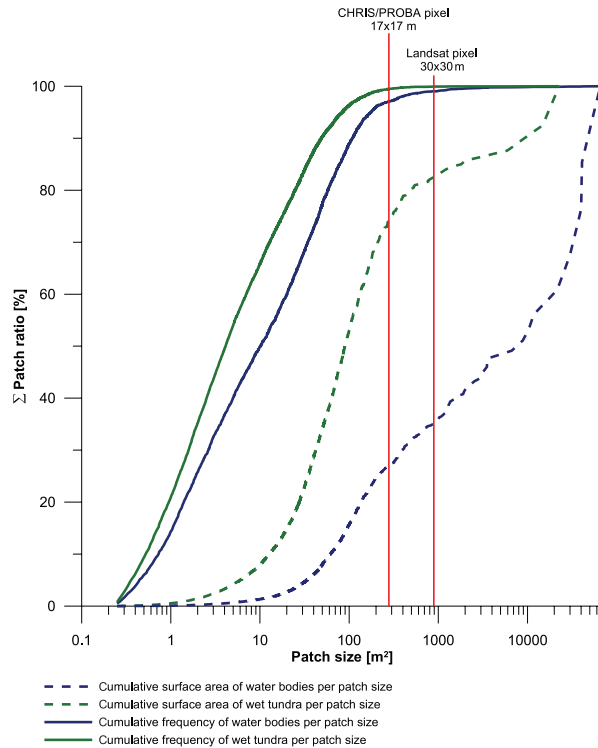

Fig. 4. Cumulative percentage plots of surface areas (broken lines) and frequencies (continuous lines) for water bodies and *wet tundra* patches. Vertical lines indicate the pixel size of CHRIS/PROBA data ($17 \times 17 \, \text{m}$) and Landsat data ($30 \times 30 \, \text{m}$).
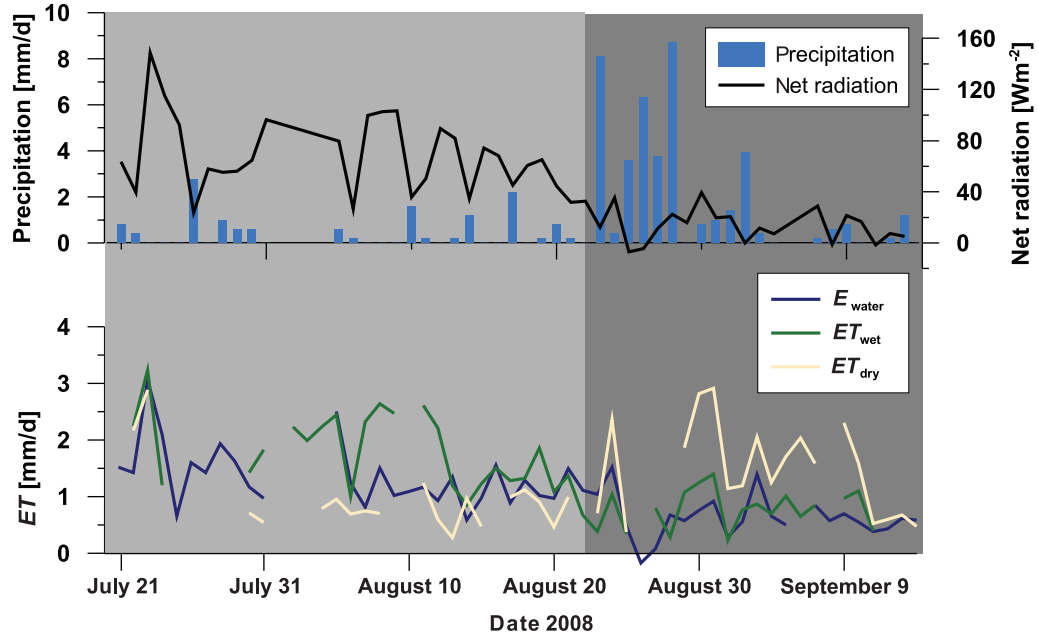
Fig. 5. Daily precipitation, net radiation and evapotranspiration (ET) from wet (*ET*wet) and *dry tundra* (*ET*dry) and evaporation from water bodies (*E*water) during the observation period from July 21 to September 14, 2008. Summer and fall are represented by light grey and dark grey backgrounds, respectively.

The average area-weighted ET rate for the whole area of ice-wedge polygonal tundra on Samoylov Island (excluding lakes larger than 0.1 ha) was 1.2 mm/d (*SD* = 0.6 mm/d). The contribution from *wet tundra*, *dry tundra* and water bodies to total landscape-scale ET varied considerably for summer and fall (Table 3). In summer, *wet tundra* and water surfaces together contributed about half to total ET of the ice-wedge polygonal tundra on Samoylov Island

(excluding lakes larger than 0.1 ha), whereas their contribution was reduced to about 20% in fall.

4.4. Downscaling mixed satellite pixels

Satellite pixels could be decomposed into their respective subpixel components by intersecting the aerial land cover and the satellite imagery classifications. A pixel-by-pixel

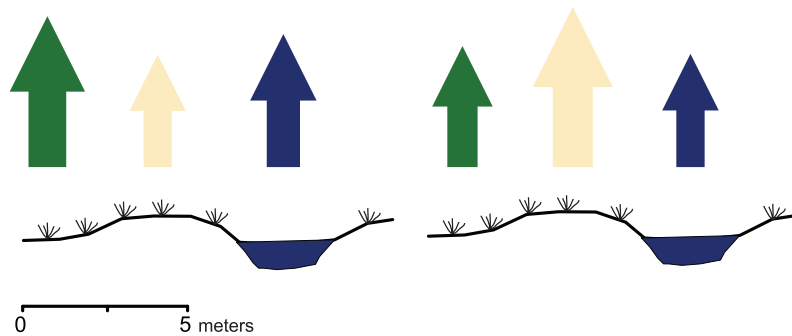|	Summer period (July 21 to August 21)			Fall period (August 22 to September 14)		
	Wet tundra	Dry tundra	Water	Wet tundra	Dry tundra	Water
average ET rate	1.8	1.0	1.4	0.8	1.4	0.7
standard deviation	1.0	0.7	0.7	0.4	0.9	0.4

Fig. 6. ET rates for *wet tundra*, *dry tundra* and water surfaces during summer and fall, as derived from plot measurements. The size of the arrows is proportional to the ET rates.
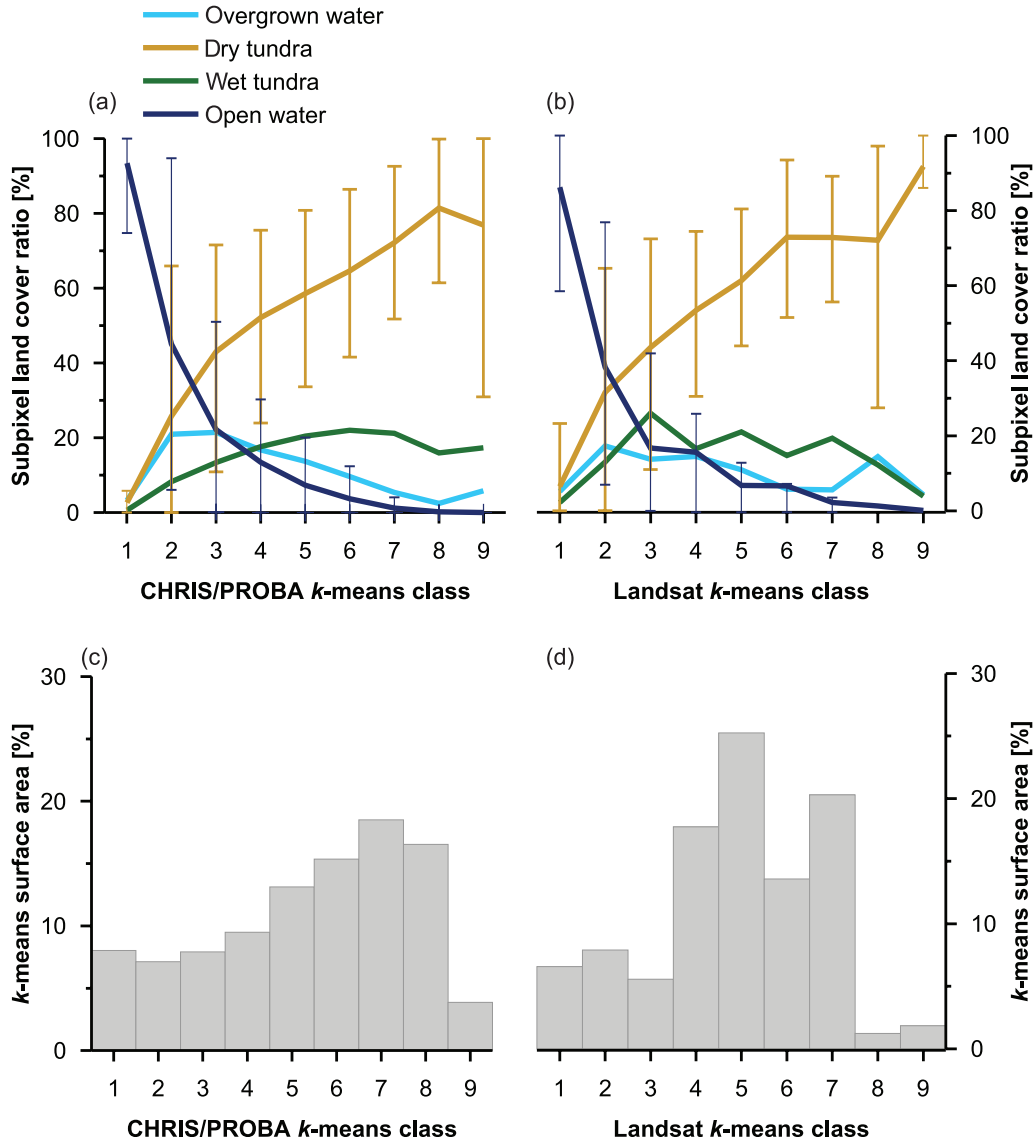
Fig. 7. Mean subpixel-scale land cover percentages for the total mapped area on Samoylov Island, shown for each *k*-means class from (a) CHRIS/PROBA data collected on July 23, 2008 and (b) Landsat-7 ETM+ collected on July 23, 2000, of the total mapped area on Samoylov Island. Vertical lines indicate the lower 10%- and the upper 90%-quantile for the relative proportions of subpixel-scale *open water* and *dry tundra*. *Open water* and *overgrown water* (quantiles not shown) show a good separability from *dry tundra* in both CHRIS/PROBA and Landsat data. Subpixel-scale ratios of *wet tundra* (quantiles not shown) can be clearly separated from the other land cover classes in Landsat but not in CHRIS/PROBA data. (c) and (d) Grey bars show the percentage of the total mapped area covered by each of the *k*-means classes for (c) CHRIS/PROBA and (d) Landsat.

analysis yielded the proportion of each aerial land cover classes within each satellite pixel (Fig. 7). Only 9% of all Landsat pixels mapped on Samoylov Island can be considered as homogeneous, containing 95% or more of one land cover type. The remaining 91% of the pixels were composed of patches or fragments of *dry tundra* and *wet tundra* as well as water surfaces.

Figure 7a and b show the ratio of each aerial land cover class in each of the nine *k*-means classes of the CHRIS/PROBA and the Landsat images. For both CHRIS/PROBA and Landsat, the spectral classification of the satellite pixels was determined by the proportions of *open water* and *dry tundra* within each pixel. Class 1 was a water class with a mean ratio of 93% *open water* for CHRIS
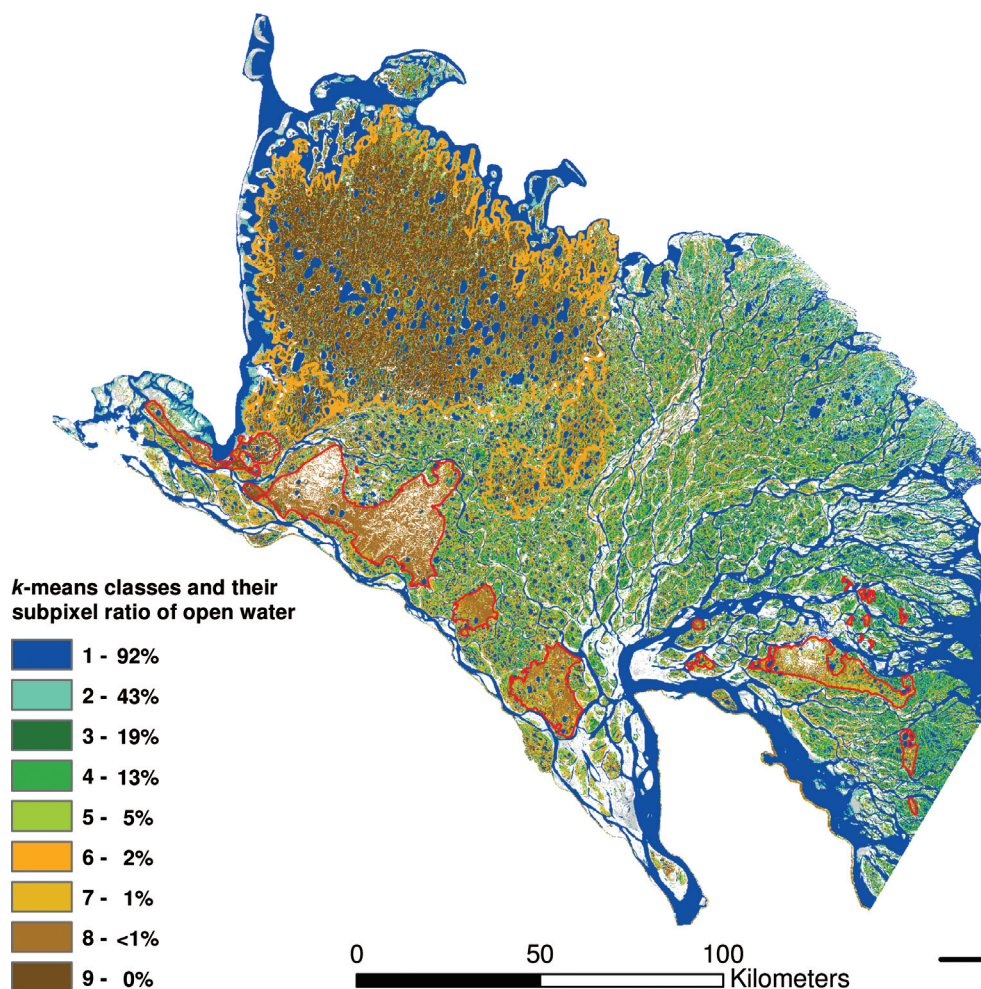
Fig. 8. Percentage of subpixel-scale *open water* for each of the nine *k*-means classes in the Lena Delta. The spectral grouping of the *k*-means classes is determined by the relative proportions of subpixel-scale *open water* versus *dry tundra* as shown in Fig. 7. White areas were not included in the classification as they are not spectrally representative of the ice-wedge polygonal tundra on Samoylov Island. Orange boundaries indicate the second terrace, red boundaries the third terrace of the Delta. The remaining area belongs to the first terrace.

PROBA and 86% for Landsat. Classes 2–9 were then characterised by a gradual decrease in *open water* and an increase in *dry tundra*. Class 1 and Class 4–10 in particular showed clear differences in the ratio of *open water* and *dry tundra*. The proportions of the different land cover types within each satellite pixel in Class 2 and Class 3, however, showed considerable variation.

Only 8% of the total mapped area on Samoylov Island could be classified as water bodies (including large thermo-karst lakes) from CHRIS/PROBA and Landsat data (Fig. 7c and d) compared to 25% from high-resolution aerial images. Over 90% of the number of both water bodies and *wet tundra* patches in the ice-wedge polygonal tundra of Samoylov Island were smaller than either the CHRIS/PROBA or the Landsat pixels (Fig. 4). Thus, 27% of the total surface area of water bodies was not resolved

by CHRIS/PROBA and 35% was not resolved by Landsat imagery. Similarly, 75% of the total surface area of *wet tundra* could not be resolved from CHRIS/PROBA data and 83% from Landsat data.

The relative proportions of the different land cover types within the satellite pixels were very similar for CHRIS/PROBA and Landsat in the *k*-means Class 1 to Class 7 (Fig. 7a and b). The main difference between the two types of imagery could be seen in Class 8 and Class 9. Class 8 showed an increasing proportion of *overgrown water* in the Landsat imagery, but this was at a minimum in the CHRIS/PROBA imagery. Landsat Class 8, however, made up only 1% of the total mapped area, and subpixel composition may therefore not have been representative (Fig. 7d). In Landsat Class 9, the proportion of *dry tundra* increased while the proportions of *wet tundra* and water

surfaces were negligible. In contrast, CHRIS/PROBA Class 9 showed a decreasing proportion of *dry tundra* and increasing proportions of *wet tundra* and water surfaces.

4.5. *Landsat subpixel heterogeneity of the Lena River Delta*

The Landsat subpixel heterogeneity, as shown in Fig. 7b, was used to assess the proportions of land and water within each Landsat pixel across the entire Lena Delta (Fig. 8). Large thermokarst lakes and Lena River channels were represented in *k*-means Class 1. With 60% water and 40% land, *k*-means Class 2 could not clearly be categorised as either a water or land class; it covered mainly riparian and coastal areas. Class 3 to Class 9, however, had proportions of about 1/3 or less water surfaces and were therefore considered to be land classes. These classes covered a total area of 12 781 km^2, which made up about 70% of the total land area in the delta. Water surfaces within Class 3 to Class 9 (as derived from Fig. 7b) amounted to an area of 1577 km^2, representing about 7% of the total land area in the delta. The area covered by water surfaces was divided into 971 km^2 *overgrown water* and 606 km^2 *open water*. The overall proportions of *dry tundra*, *wet tundra* and water surfaces within Landsat pixels for the entire Lena Delta were similar to those for ice-wedge polygonal tundra on Samoylov Island (Table 3).

The distribution of the *k*-means classes within the Lena Delta reflected the main geomorphological terraces (Fig. 8). Class 9 dominated the second terrace in the north-western part of the delta, whereas the third terrace was characterised by Class 9 together with Class 8, both of which have little or no subpixel-scale heterogeneity. The first terrace, in the central and eastern part of the delta, was dominated by Class 3 to Class 7, which had high proportions of water surfaces and *wet tundra*, and was therefore likely to indicate the presence of polygonal tundra. These classes occupied an area of 6192 km^2, representing about 30% of the total land area of the delta.

We tested the downscaling approach in an area in the south-western part of the Lena Delta, in which Grosse et al. (2008) mapped about 239 ha of small open water bodies (0.003–0.1 ha) from panchromatic SPOT-5 data with a 2.5 m resolution. Decomposing composite Landsat pixels via the downscaling function in this study yielded 88 ha of *open water* and 305 ha of combined *open water* and *overgrown water*.

5. Discussion

5.1. *Plot-scale ET characteristics*

Plot measurements of ET were successfully scaled to eddy covariance measurements. The total ET of 1.2 mm/d for ice-wedge polygonal tundra on Samoylov Island using lysimeter measurements and evaporation modelling is well within the range of previously reported values for poly-gonal tundra, which lie between 1.0 and 1.8 mm/d (Eugster et al., 2000). Summer ET rates (July–August) of *wet tundra* and *dry tundra* found in this study are in good agreement with the values presented by Langer et al. (2011a), who found ET rates of 1.0 mm/d ($SD = 1.1$ mm/d) for *dry tundra* and 2.2 mm/d ($SD = 1.1$ mm/d) for *wet tundra* for a period from June to August. The summer evaporation rate from water surfaces of 1.4 mm/d in this study falls at the lower range of values reported in other studies on the Alaskan coastal plain (2.0–2.3 mm/d) (Kane and Carlson, 1973; Rovansek et al., 1996; Mendez et al., 1998) and in Canada (4.4 mm/d) (Roulet and Woo, 1986; Marsh and Bigras, 1988), which is most likely explained by the higher values of net radiation at these more southerly study sites.

In summer, *wet tundra* and water bodies on Samoylov Island show higher ET rates than *dry tundra*. The differences in summer ET rates seem to be primarily controlled by the combination of high net radiation and low precipitation, which has also been pointed out by other studies on Samoylov Island (Boike et al., 2008; Langer et al., 2011a) and at other locations on the Arctic coastal plain (Liljedahl et al., 2011). The tundra at the study site is dominated by mosses, which can strongly control the water vapour flux at the surface (Rouse, 2000; Grant et al., 2003; McFadden et al., 2003). Mosses lack stomatal control of water loss (Oechel and Sveinbjörnsson, 1978). They there-fore evaporate freely, provided they are moist (Rouse, 2000; Thompson et al., 2004). Rates of water loss from a saturated moss canopy can be comparable or even higher than those from a free water surface (Firbas, 1931; Barkman, 1958), which explains the magnitude of evapora-tion from water surfaces being similar to that from *wet tundra* in summer and fall. *Wet tundra* in the low-lying ice-wedge polygonal centres stays saturated throughout sum-mer and fall due to the near-surface water level, while *dry tundra* on the elevated polygonal rims relies mostly on precipitation for moisture input. This likely explains the difference in ET rates during the summer, when the combination of high net radiation and little precipitation limits ET from *dry tundra*.

In fall, the difference between ET from *dry tundra* and *wet tundra* as well as water bodies is reversed with ET from

dry tundra being about 40% higher than from both *wet tundra* and water bodies. This result suggests other limitations than net radiation and near-surface soil moisture on local ET rates during fall. The large differences in the latent heat fluxes between *dry tundra* on the elevated polygon rims and *wet tundra* in the low-lying ice-wedge polygon centres indicate instead considerable differences in the surface energy balance during fall. The rims feature a higher albedo than the lowered centres (Langer et al., 2011a) and almost a similar average surface temperature (Langer et al., 2010). Therefore, it can be excluded that the increased latent heat flux originates from a larger radiation budget at the rims. Furthermore, the potential differences in ground heat flux between the polygon rims and centres are negligible in fall (about $6\,W/m^2$) (Langer et al., 2010, 2011a) and can therefore not account solely for the difference in ET rates, as suggested by Liljedahl et al. (2011). We conclude that there must be differences in the partitioning of sensible and latent heat fluxes between the polygonal rims and centres. The energy partitioning of sensible and latent heat fluxes is potentially triggered by differences in the surface-air temperature gradients, in the saturation vapour pressure deficit between the surface and the air, or in the resistance to ET. However, frequent and high precipitation during the fall period renders the moss canopy of *dry tundra* on the rims equally wet as *wet tundra* in the water-saturated polygonal centres. The rims feature a considerably higher surface roughness than the water-saturated polygonal centres due to the dendritic growth form of the dominant moss species (*Hylocomium splendens*). This difference in growth form of the mosses can strongly modify water loss from the moss canopy (Tallis, 1959; Hosokawa et al., 1964) and potentially lower the resistance to ET on the rims. Additionally, the elevated polygonal rims are more exposed to wind, all of which could lead to generally increased turbulent heat fluxes at the polygonal rims with a shift towards higher latent heat fluxes.

5.2. Downscaling land cover

The distribution of *k*-means classes are similar in both CHRIS/PROBA and Landsat imagery. This suggests that the underlying land cover fractions did not vary significantly between the different acquisition dates. The mean proportions of land cover types within each *k*-means spectral class show a similar trend for different dates, sensors and resolutions. However, the proportions of the different land cover types within *k*-means Class 2 and Class 3 show a large degree of variability for both CHRIS/PROBA and Landsat data. In these classes, the same spectral signature can result from various combinations of the underlying subpixel-scale land cover composition. This subject requires further investigation in other representative parts of the delta, on the basis of very high-resolution satellite and radar imagery (resolution less than 4 m).

The high degree of variability in the relative proportions of different land cover types in CHRIS/PROBA Class 9 suggests that the high NIR reflectance from short but dry surfaces and also high NIR reflectance from tall but wet vegetation cannot be distinguished using CHRIS/PROBA data. With the additional surface information available from two SWIR bands, Landsat data is more effective in distinguishing between those dry and wet tundra surfaces. Further investigations regarding the spectral mixing of Arctic land surfaces within coarse-scale resolution satellite data are required to fully understand the physical aspects of the downscaling scheme presented in this study and its applicability to other satellite sensors.

The distribution of *k*-means classes within the delta and their associated subpixel-scale composition is in overall agreement with the observations from other studies. Polygonal tundra is primarily found on the first terrace in the central and eastern part of the delta, whereas the north-western part of the delta is dry (Schneider et al., 2009; Ulrich et al., 2009) and appears more homogeneous with little or no subpixel-scale heterogeneity. In an area in the southwest Lena River Delta along the Olenek channel, Grosse et al. (2008) mapped 239 ha small open water bodies, while this study estimated an area of 305 ha water surfaces, of which 88 ha was *open water*. The differences are probably not due to inter-annual differences in the surface hydrology, as the accumulated precipitation up to the image acquisition dates in 2001 and 2006 only differs by 9 mm, which is unlikely to have caused significant differences in the extent of water surfaces. Differences in the classification of water surfaces might be due to the different spectral ranges of the imagery used for classification (panchromatic versus VNIR) or differences in surface properties of land cover at the site investigated by Grosse et al. (2008) and on Samoylov Island. Differences in surface properties, e.g. the ratio of shrub cover, are likely to affect the spectral characteristics of composite Landsat pixels and associated subpixel-scale estimates of land/water cover, which underlines the importance of detailed field studies to further improve the presented scaling approach.

Misclassifications of the heterogeneous ice-wedge polygonal tundra can occur due to a limited spectral range of the aerial or satellite imagery used for high-resolution land cover mapping. Furthermore, special care must be taken when selecting the study area to ensure that it produces a representative dataset of the subpixel-scale heterogeneity of the landscape in question. In this study, we have been able to show the range of variability in the underlying land cover classes by decomposing each single Landsat pixel, rather than merely looking at the study area as a whole.

We could then assign the average proportion of the different land cover types to each spectral class in the satellite data. This empirical downscaling of land cover can be used where standard spectral mixing analyses (SMA) are not successful. SMA procedures rely on the selection of endmembers, i.e. pixels with completely homogeneous land cover. However, the high level of heterogeneity in the ice-wedge polygonal landscape makes it difficult and in the case of *overgrown water* even impossible to select suitable endmembers. In this study, we have therefore used the mean proportions of each land cover type within each *k*-means class to decompose the composite pixels. Further developments include the use of probability distribution functions (PDFs) that ensure the mean, standard deviation and skew of the subpixel-scale variability when disaggregating coarse resolution data (Hill et al., 2011). The success of this approach, however, depends on the quality of the subpixel-scale PDF used: 'The PDF must capture the natural heterogeneity at a sufficiently fine resolution to preserve critical ecosystem states and processes' (Hill et al., 2011). Extrapolation of the PDF to larger regions requires the PDF to be spatially representative. In regions with similar land cover types and spectral properties to the ice-wedge polygonal tundra, we would expect to find similar PDFs to those presented in this study. Extending our approach to coarser resolution imagery (e.g. MERIS with 1 km resolution) would mean including land cover types, e.g. flood plains and barren ground, which have different spectral signatures from those exhibited by ice-wedge polygonal tundra.

5.3. Implications of subpixel-scale heterogeneity

Spectral information from Landsat imagery can effectively determine the subpixel-scale percentages of *dry tundra* and *open water* surfaces. Some 13% of the delta's land surface (not including rivers and coastal areas) has been estimated from Landsat data to be occupied by water bodies. However, by including the subpixel-scale land/water fraction, the water surface area increases to 20%. Classifications based on traditional Landsat analyses may therefore underestimate the water surface area by a factor of 1.5. Databases on even larger scales, such as the Global Lakes and Wetland Database (GLWD) by Lehner and Döll (2004), could underestimate the water surface area of the Lena Delta by a factor of 4. Similar discrepancies have been found by Grosse et al. (2008) who estimated the water surface area detected by high-resolution remote sensing data over three sites in eastern Siberia to be 2–7 times larger than those indicated by the GLWD. Assuming the polygonal tundra of Samoylov Island to be representative of the *wet sedge- and moss-dominated tundra* in the Lena Delta as a whole [as classified by Schneider et al. (2009)],

we estimate the existence of approximately 6 200 000 small water bodies (smaller than 0.1 ha) to exist in the *wet sedge- and moss-dominated tundra* within an area of 8277 km^2.

The land cover class *overgrown water* shows the largest variation within our high-resolution aerial land cover classification. This is probably due to the different dates of image acquisition and field mapping, with misclassified sites representing transient water accumulations. *Wet tundra*, *overgrown water* and *open water* bodies represent stages in a landscape sequence that are dependent on the current water level. Their transient nature makes them prone to changes in the inter-annual and seasonal surface moisture regime (Smol and Douglas, 2007; Boike et al., 2008), which presents a key challenge when incorporating temporal changes of fine-scale land cover into the modelling of water, heat and carbon fluxes.

The proportions of ET from *wet tundra*, *dry tundra* and water bodies varied considerably for summer and fall. The results on ET of this study can be generalised to the surface energy balance, which is a key element in larger-scale atmospheric models. For polygonal tundra on Samoylov Island, a distinctly different surface energy balance depending on the land cover class has been demonstrated both during summer and winter (Langer et al., 2011a, b), so that it should be calculated independently in modelling approaches. In the case of carbon fluxes, differences between land cover types of ice-wedge polygonal tundra are much higher than for ET (Kutzbach et al., 2004; Sachs et al., 2010), which makes correct fine-scale land cover classifications even more important. *Wet tundra* and *overgrown water* show methane fluxes that are up to 40 and 20 times higher, respectively, than *dry tundra* and *open water* (Sachs et al., 2010). In this case, misclassifications of land cover at the metre scale can result in large errors at the landscape scale. Schneider et al. (2009), for example, find a much higher water body ratio (30%) and a much lower ratio of *wet tundra* (8%) for ice-wedge polygonal tundra on Samoylov Island as compared to this study (16% and 19%). Their land cover classification would lead to an underestimation of the areally weighted methane flux by about 40%.

The classification techniques presented in this study can be used to compile improved fractional distributions for land cover classes within a larger-scale grid, which will facilitate upscaling of the surface energy balance as well as carbon fluxes computed for individual land cover types. A further improvement in the method would include the statistical representation of temporal changes in land cover. It should be emphasised that this approach would account for subpixel-scale heterogeneity in the land cover on a metre scale, simply by reproducing the correct land/water cover statistics within a grid cell.

The preceding discussion highlights the importance of integrating detailed field studies, multi-scale remote sensing data and model schemes in Arctic areas. Such integrated studies would be able to account for highly heterogeneous land cover patterns in large-scale models (Rietkerk et al., 2011), to monitor fine-scale changes of land surface properties (Stow et al., 2004) and to validate existing land cover classifications, especially with regard to the extent of water bodies and wetlands (Frey and Smith, 2007).

6. Conclusions

Resolutions of 4 m or less are necessary in order to map the fine-scale landscape elements of ice-wedge polygonal tundra. Land cover elements of ice-wedge polygonal tundra are therefore not resolved by CHRIS/PROBA and Landsat imagery, and any coarser-scale land cover databases. About 90% of the satellite pixels are composed of patches or fragments of *dry tundra* and *wet tundra* as well as water surfaces. Spectral classification of composite CHRIS/PROBA and Landsat pixels in areas of ice-wedge polygonal tundra is determined by the relative proportions of *dry tundra* and water within each pixel. Decomposition of composite pixels is therefore possible using sub-metre resolution imagery in the visible and near-infrared to derive subpixel-scale probabilities of land/water cover. The actual land/water proportions within each composite pixel are most effectively captured by Landsat data, which provide more surface information in the SWIR range. The inclusion of subpixel-scale water bodies increases the water surface area of the total land area in the Lena Delta from 13 to 20%. This approach, however, is sensitive to the specific surface spectral characteristics of the subpixel-scale land/water covers. In order to ensure the validity of these subpixel-scale probabilities, fine-scale land cover mapping must capture the typical heterogeneity of all the relevant land cover classes. Also, further high-resolution analyses of other typical tundra and wetland areas in permafrost landscapes are necessary.

The land cover types of ice-wedge polygonal tundra exhibit distinctly different seasonal differences in water, carbon and energy fluxes, which should be calculated independently in modelling approaches. The classification and scaling techniques presented in this study take into account the subpixel-scale heterogeneity of ice-wedge polygonal tundra from mid-summer to late fall on the metre scale. They simply reproduce the actual land cover statistics within a pixel, which can be considered as a prerequisite for reliable large-scale modelling of water, energy and carbon exchange from permafrost areas.

References

Barkman, J. 1958. *Phytosociology and Ecology of Cryptogamic Epiphytes: Including a Taxonomic Survey and Description of their Vegetation Units in Europe*. Van Gorcum, Assen.

Boike, J., Wille, C. and Abnizova, A. 2008. Climatology and summer energy and water balance of polygonal tundra in the Lena River Delta, Siberia. *J. Geophys. Res.* **113**(G03025), DOI:10.1029/2007JG000540

Bonan, G., Chapin III, F. and Thompson, S. 1995. Boreal forest and tundra ecosystems as components of the climate system. *Clim. Chang.* **29**(2), 145–167.

Braun-Blanquet, J. 1932. *Plant Sociology. The Study of Plant Communities*. 1st ed. McGraw-Hill, New York.

Chapin III, F., Sturm, M., Serreze, M., McFadden, J. P., Key, R. J. and co-authors. 2005. Role of land-surface changes in Arctic summer warming. *Science* **310**(5748), 657–660.

Chapin III, F. S., McGuire, A. D., Randerson, J., Pielke, R., Baldocchi, D. and co-authors. 2000. Arctic and boreal ecosystems of western North America as components of the climate system. Glob. *Change Biol.* **6**(S1), 211–223.

Eugster, W., Rouse, W., Pielke Sr, R., Mcfadden, J., Baldocchi, D. and co-authors. 2000. Land-atmosphere energy exchange in Arctic tundra and boreal forest: available data and feedbacks to climate. *Glob. Change Biol.* **6**(S1), 84–115.

Euskirchen, E. S. and Bret-Harte, M. S. 2009. The arctic observatory network. *FluxLetter* **2**(2), 1–3.

Firbas, F. 1931. *Untersuchungen über den Wasserhaushalt der Hochmoorpflanzen*. Gebrüder Borntraeger, Leipzig.

French, H. 2007. *The Periglacial Environment*. 3rd ed. Wiley, West Sussex.

Frey, K. and Smith, L. 2007. How well do we know Northern land cover? Comparison of four global vegetation and wetland products with a new ground-truth database for West Siberia. Glob. *Biogeochem. Cycles* **21**(1), 15 pp. GB1016.

Garratt, J. 1994. *The Atmospheric Boundary Layer*. Cambridge University Press, Cambridge.

Gómez-Chova, L., Alonso, L., Guanter, L., Camps-Valls, G., Calpe, J. and co-authors. 2008. Correction of systematic spatial noise in push-broom hyperspectral sensors: application to CHRIS/PROBA images. *Appl. Opt.* **47**(28), F46–F60.

Grant, R., Oechel, W. and Ping, C. 2003. Modelling carbon balances of coastal Arctic tundra under changing climate. *Glob. Change Biol.* **9**(1), 16–36.

Grigoriev, M. 1993. *Cryomorphogenesis in the Lena Delta* (in Russian). Permafrost Institute Press, Yakutsk.

Grigoriev, N. 1960. The temperature of permafrost in the Lena delta basin – deposit conditions and properties of the permafrost in Yakutia, *Yakutsk* **2**, 97–101 (in Russian).

Grosse, G., Romanovsky, V., Walter, K., Morgenstern, A., Lantuit, H. and co-authors. 2008. Distribution of thermokarst lakes and ponds at three yedoma sites in Siberia. In *Ninth International Conference on Permafrost* (eds. D. L. Kane and K. M. Hinkel), Institute of Northern Engineering, University of Alaska Fairbanks, pp. 551–556.

Guanter, L., Richter, R. and Moreno, J. 2006. Spectral calibration of hyperspectral imagery using atmospheric absorption features. *Appl. Opt*. **45**(10), 2360–2370.

Gutowski, W. J., Wei, H., Voeroesmarty, C. J. and Fekete, B. M. 2007. Influence of Arctic wetlands on Arctic atmospheric circulation. *J. Climate* **20**(16), 4243–4254.

Hill, T., Quaife, T. and Williams, M. 2011. A data assimilation method for using low-resolution Earth observation data in heterogeneous ecosystems. *J. Geophys*. Res. **116**(D8), 12 pp. D08117.

Hinzman, L. D., Bettez, N. D. and Bolton, W. R. E. A. 2005. Evidence and implications of recent climate change in Northern Alaska and other Arctic regions. *Clim. Chang*. **72**, 251–298.

Hosokawa, T., Odani, N. and Tagawa, H. 1964. Causality of the distribution of corticolous species in forests with special reference to the physio-ecological approach. *The Bryologist* **67**(4), 396–411.

Kane, D. and Carlson, R. 1973. *Hydrology of the Central Arctic River Basins of Alaska*. Institute of Water Resources, University of Alaska, Report IWR-41.

Kattsov, V., Walsh, J., Chapman, W., Govorkova, V., Pavlova, T. and co-authors. 2007. Simulation and projection of Arctic freshwater budget components by the IPCC AR4 global climate models. *J. Hydrometeorol*. **8**(3), 571–589.

Kutzbach, L., Wagner, D. and Pfeiffer, E.-M. 2004. Effect of microrelief and vegetation on methane emission from wet polygonal tundra, Lena Delta, Northern Siberia. *Biogeochemistry* **69**, 341–362.

Langer, M., Westermann, S. and Boike, J. 2010. Spatial and temporal variations of summer surface temperatures of wet polygonal tundra in Siberia – implications for MODIS LST based permafrost monitoring. *Remote Sens. Environ*. **114**(9), 2059–2069.

Langer, M., Westermann, S., Muster, S., Piel, K. and Boike, J. 2011a. The surface energy balance of a polygonal tundra site in Northern Siberia – part 1: spring to fall. *The Cryosphere* **5**, 151–171.

Langer, M., Westermann, S., Muster, S., Piel, K. and Boike, J. 2011b. Permafrost and surface energy balance of a polygonal tundra site in Northern Siberia – part 2: winter. *The Cryosphere* **5**, 509–524.

Legendre P. 2001. Program K-means user's guide. *Departement des Sciences Biologique Univ. de Montreal. Montreal*; 11 pp.

Lehner, B. and Döll, P. 2004. Development and validation of a global database of lakes, reservoirs and wetlands. *J. Hydrol*. **296**(1–4), 1–22.

Liljedahl, A. K., Hinzman, L. D., Harazono, Y., Zona, D., Tweedie, C. E. and co-authors. 2011. Nonlinear controls on evapotranspiration in arctic coastal wetlands. *Biogeosciences* **8**(11), 3375–3389. DOI:10.5194/bg-8-3375-2011

Lillesand, T., Kiefer, R. and Chipman, J. 2004. *Remote Sensing and Image Interpretation*. 5th ed. Wiley, New York.

MacKay, D. 2003. *Information Theory, Inference, and Learning Algorithms*. Cambridge University Press, Cambridge.

Marsh, P. and Bigras, S. 1988. Evaporation from Mackenzie delta lakes, NWT, Canada. *Arctic Alpine Res*. **20**(2), 220–229.

Mauder, M. and Foken, T. 2004. Documentation and instruction manual of the eddy covariance software package TK2. University of Bayreuth, Bayreuth.

Mauder, M., Foken, T., Clement, R., Elbers, J., Eugster, W. and co-authors. 2008. Quality control of CarboEurope flux data? Part 2: inter-comparison of eddy-covariance software. *Biogeosciences* **5**(2), 451–462.

Mauder, M., Liebethal, C., Göckede, M., Leps, J., Beyrich, F. and co-authors. 2006. Processing and quality control of flux data during LITFASS-2003. *Boundary-Layer Meteorol*. **121**(1), 67–88.

McFadden, J. P., Eugster, W. and Chapin III, F. S. 2003. A regional study of the controls on water vapor and CO_{rm2} exchange in Arctic tundra. *Ecology* **84**(10), 2762–2776.

McGuire, A., Chapin III, F., Wirth, C., Apps, M., Bhatti, J. and co-authors. 2007. Responses of high latitude ecosystems to global change: potential consequences for the climate system. (eds. J. G. Canadell, D. E. Pataki, and L. F. Pitelka), *Terrestrial ecosystems in a changing world*. The IGBP Series. Springer-Verlag, Berlin, Germany, 297–310.

Mendez, J., Hinzman, L. and Kane, D. 1998. Evapotranspiration from a wetland complex on the Arctic coastal plain of Alaska. *Nordic Hydrol*. **29**(4), 303–330.

Morgenstern, A., Grosse, G. and Schirrmeister, L. 2008. Genetic, morphological, and statistical characterization of lakes in the permafrost-dominated Lena Delta. In: *Proceedings of the Ninth International Conference on Permafrost (NICOP), June 29–July 3, 2008*, Fairbanks, Alaska, USA.

Naumov, Y. 2004. Soils and soil cover of Northeastern Eurasia. *Cryosols*: Permafrost-affected soils, p. 161.

Oechel, W. C. and Sveinbjörnsson, B. 1978. Primary production processes in Arctic bryophytes at Barrow, Alaska, *Vegetation and Production Ecology of an Alaskan Arctic Tundra*, 269–298.

Ping, C., Clark, M. and Swanson, D. 2004. Cryosols in Alaska. *Cryosols: Permafrost-affected soils*.

Rietkerk, M., Brovkin, V., van Bodegom, P., Claussen, M., Dekker, S. C. and co-authors. 2011. Local ecosystem feedbacks and critical transitions in the climate. *Ecological Complexity*, **8**(3), 223-228.

Roulet, N. T. and Woo, M. 1986. Wetland and lake evaporation in the low Arctic. *Arctic Alpine Res*. **18**(2), 195–200.

Rouse, W. R. 2000. The energy and water balance of high-latitude wetlands: controls and extrapolation. *Glob. Change Biol*. **6**(S1), 59–68.

Rouse, W. R., Blyth, E. M., Crawford, R. W., Gyakum, J. R., Janowicz, J. R. and co-authors. 2003. Energy and water cycles in a high-latitude, North-flowing river system. *Bull. Am. Meteorol. Soc*. **84**, 73–87.

Rovansek, R., Hinzman, L. and Kane, D. 1996. Hydrology of a tundra wetland complex on the Alaskan Arctic Coastal Plain, USA. *Arctic Alpine Res.* **28**(3), 311–317.

Sachs, T., Giebels, M., Boike, J. and Kutzbach, L. 2010. Environmental controls on CH_4 emission from polygonal tundra on the microsite scale in the Lena river delta, Siberia. *Glob. Change Biol.* **16**(11), 3096–3110.

Salmun, H., Molod, A., Albrecht, J. and Santos, F. 2009. Scales of variability of surface vegetation: calculation and implications for climate models. *J. Geophys. Res.* **114**(G2), G02007.

Schmid, H. 1994. Source areas for scalars and scalar fluxes. *Boundary-Layer Meteorol.* **67**(3), 293–318.

Schneider, J., Grosse, G. and Wagner, D. 2009. Land cover classification of tundra environments in the Arctic Lena Delta based on Landsat 7 ETM+ data and its application for upscaling of methane emissions. *Remote Sens. Environ.* **113**, 380–391.

Schwamborn, G., Rachold, V. and Grigoriev, M. 2002. Late quaternary sedimentation history of the Lena Delta. *Quat. Int.* **89**(1), 119–134.

Serreze, M. C., Bromwich, D. H., Clark, M. P., Etringer, A. J., Zhang, T. and co-authors. 2003. Large-scale hydro-climatology of the terrestrial Arctic drainage system. *J. Geophys. Res.* **108**(D2), 8160.

Serreze, M. C., Walsh, J. E., Chapin III, F. S., Osterkamp, T., Dyurgerov, M. and co-authors. 2000. Observational of recent change in the Northern high-latitude environment. *Clim. Chang.* **46**, 159–207.

Smol, J. P. and Douglas, M. S. V. 2007. Crossing the final ecological threshold in high Arctic ponds. *Proc Natl Acad Sci USA* **104**, 12395–12397. www.pnas.org/cgi/doi/10.1073/pnas.0702777104.

Sonntag, D. 1990. Important new values of the physical constants of 1986, vapour pressure formulations based on the ITS-90, and psychrometer formulae. *Zeitschrift für Meteorologie* **40**(5), 340–344.

Stow, D. A., Hope, A., McGuire, D., Verbyla, D. and Gamond, J. 2004. Remote sensing of vegetation and land-cover change in Arctic tundra ecosystems. *Remote Sens. Environ.* **89**, 281–308.

Sturm, M., Racine, C. and Tape, K. 2001. Climate change: increasing shrub abundance in the Arctic. *Nature* **411**(6837), 546–547.

Tallis, J. 1959. Studies in the biology and ecology of rhacomitrium lanuginosum brid: II. Growth, reproduction and physiology. *J. Ecol.* **46**(2), 325–350.

Tarnocai, C. and Zoltai, S. C. 1988. *Wetlands of Arctic Canada.* In: Wetlands of Canada, Chapter 2, 29-53, National Wetlands Working Group, Canada Committee on Ecological Classification. Polyscience Publications Inc., Montreal, Quebec.

Thompson, C., Beringer, J., Chapin III, F. S. and McGuire, A. 2004. Structural complexity and land-surface energy exchange along a gradient from Arctic tundra to boreal forest. *J. Veg. Sci.* **15**, 397–406.

Ulrich, M., Grosse, G., Chabrillat, S. and Schirrmeister, L. 2009. Spectral characterization of periglacial surfaces and geomorphological units in the Arctic Lena Delta using field spectrometry and remote sensing. *Remote Sens. Environ.* **113**(6), 1220–1235.

Walker, D. A., Epstein, H. E., Romanovsky, V. E., Ping, C. L., Michaelson, G. J. and co-authors. 2008. Arctic patterned-ground ecosystems: a synthesis of field studies and models along a North American Arctic transect. *J. Geophys. Res.* **113**, G03S01.

Walker, D., Raynolds, M., Daniëls, F., Einarsson, E., Elvebakk, A. and co-authors. 2005. The circumpolar Arctic vegetation map. *J. Veg. Sci.* **16**(3), 267–282.

White, D., Hinzman, L., Alessa, L. F., Cassano, J., Chambers, M. and co-authors. 2007. The Arctic freshwater system: changes and impacts. *J. Geophys. Res.* **112**(G4), G04S54.

Woo, M.-K., Kane, D., Carey, S. and Yang, D. 2008. Progress in permafrost hydrology in the new millennium. *Permafrost Periglacial Process.* **19**, 237–254.